Phys. Med. Biol., 1990, Vol. 35, No 4, 517–538. Printed in the UK

An analytic theory of the point-source non-uniformity correction factor for thick-walled ionisation chambers in photon beams

Alex F Bielajew

Division of Physics, Ionizing Radiation Standards, National Research Council of Canada, Ottawa, Canada K1A 0R6

Received 6 June 1989, in final form 26 September 1989

Abstract. In exposure and air kerma measurements, axial and radial non-uniformity perturbation correction factors are used to account for the non-uniformity of the incident photon field in the vicinity of the ionisation chamber cavity. An analytic theory for calculating the point source non-uniformity correction factor for thick-walled ionisation chambers is developed. The theory developed herein is compared with Monte Carlo calculations for chambers with pancake, cylindrical and spherical geometries similar in size to the instruments employed by Standards laboratories. The agreement between Monte Carlo calculations and the analytic theory is excellent and demonstrates the viability of the analytic theory at large and small source to chamber distances. The perturbations, which differ from those calculated or measured by some Standards laboratories, suggest that corrections of the order of 0.3% should be applied to typical pancake geometries, smaller corrections of the order of 0.05% or less for typical Farmer-type chambers, and no correction for spherical chambers. The analytic theory predicts chamber geometries which can either minimise or maximise the effect of point source non-uniformity. An experiment is described that would measure the correction with good accuracy.

1. Introduction

When a detector is placed in the field of a radiation source, the point at which the radiation field is being measured is uncertain, owing to the finite size of the detector. In the realm of exposure or air kerma measurement performed in Standards laboratories, one usually assumes that the 'point of measurement' is at the geometric centre of the chamber and the correction for the departure in ion chamber response from the inverse-square law is accounted for by the 'axial' and 'radial' non-uniformity correction factors, k_{an} and k_{rn}, respectively. The axial factor is a correction for the non-uniformity of the photon field along the line from the source through the cavity centre while the radial factor accounts for non-uniformity in the transverse direction. The radial correction also accounts for the transverse field non-uniformity due to finite-size source effects and scatter from the collimator and room.

There are divergent views as to how the correction for point source non-uniformity is to be applied (Gray 1937, Failla and Marinelli 1937, Mayneord and Roberts 1937, Spiers 1941, Burlin 1959, Kondo and Randolph 1960, Boutillon and Niatel 1973, Loftus and Weaver 1974, W H Henry as reported in Shortt and Ross 1986). For example, the BIPM (Bureau International des Poids et Mesures, France) ^{60}Co-exposure standard has a calculated correction of 0.9968 ± 0.0020 (Boutillon and Niatel 1973) for the axial

portion of the non-uniformity correction. In a similar fashion, the axial corrections for the PTB (Physikalisch-Technische Bundesanstalt, Germany) ^{60}Co-exposure standards fall in the range 0.9925±0.0015–0.9955±0.0015, depending upon which of their three standard chambers is used (Niatel *et al* 1975). However, at NIST (National Institute for Science and Technology, USA, formerly NBS (National Bureau of Standards)), and the NRCC (National Research Council, Canada), no correction is attributed to point source non-uniformity although uncertainties of 0.1% and 0.2%, respectively, are assigned (Loftus and Weaver 1974, Shortt and Ross 1986). This latter view has had some theoretical and experimental support(Gray 1937, Spiers 1941, Burlin 1959, Kondo and Randolph 1960).

In view of the differing opinions, this question is addressed anew aided by Monte Carlo methods to serve as a calculational tool along with the employment of a formal (calculable only by Monte Carlo methods) theory of point source non-uniformity correction (Bielajew 1990) that is based on a consistent theoretical framework describing thick-walled ion chamber response (Bielajew 1986). If one sought to calculate the correction factor by Monte Carlo methods to much better than 0.1% at distances typical of standardisation calibrations, hundreds of hours of CPU time would be required on even the fastest computers available (Bielajew 1990). To aid with the interpretation of the Monte Carlo results at large distances, an approximate analytic theory is developed that extends the work of Kondo and Randolph (1960). The theory developed herein demonstrates excellent agreement with Monte Carlo calculations and one may conclude that it may be used to predict the point source non-uniformity corrections to within 0.1% for small chambers at all reasonable (a metre or so) source to chamber distances.

2. The theory

Kondo and Randolph express their correction for point source non-uniformity, A_{pn}, as

$$A_{pn} = \frac{r_0^2}{4\pi V_{cav}} \int \frac{dA_1}{r^2} \int dA_2 \frac{\cos\psi_{21} \cos\psi_{12}}{h} \tag{1}$$

where r_0 is the distance from the point source to the centre of the chamber, V_{cav} is the volume of the cavity, dA_1 and dA_2 are surface elements of the cavity, r is the distance from the source to the surface element dA_1, h is the distance between dA_1 and dA_2, $\cos\psi_{12}$ is the cosine the h-line makes with the inward normal from dA_1, and $\cos\psi_{21}$ is the cosine the h-line makes with the inward normal from dA_2. The essential assumptions made in deriving (1) were:

(i) the electrons entering the cavity are set in motion at the surface of the cavity,
(ii) the electrons travel through the cavity in straight lines,
(iii) the electrons deposit energy in proportion to their track length through the cavity,
(iv) the photons suffer no appreciable attenuation in passing through the chamber,
(v) the angular distribution of the electrons entering the cavity is isotropic, and
(vi) the cavity shapes are assumed to be either spheres or right cylinders excluding electrodes and guard areas.

Assumption (i) should produce accurate results if the electron range within the walls is much smaller than r_0 and the size of the cavity. This is easily satisfied for almost

all practical situations. The effect being calculated depends on the variation of r^2 over the points at which the electron is set in motion and the effect of electron drift on the effective r^2 can usually be neglected. Assumption (ii) is valid if the cavity is 'small' for most of the electrons that enter the cavity. This assumption breaks down for the low energy electrons whose range approaches the characteristic size of the cavity. Assumption (iii) neglects the increased stopping power of lower energy electrons entering the cavity but it should not matter if assumptions (ii) and (v) strictly hold. Assumption (iv) can be relaxed by including known wall attenuation and scatter corrections which can change as a function of r_0 (Bielajew 1990). Assumption (v) cannot really be justified except at extremely low energies where photoelectric interactions and strong multiple scattering cause the electron distributions to be nearly isotropic. Assumption (vi) is not a fundamental restriction but it makes the mathematical decomposition of (1) realisable. As long as the volume of the guard areas or electrodes are small compared to the volume of the cavity this assumption should be valid. Kondo and Randolph recognised the shortcoming of assumptions (iv) and (v) but remarkably, their theory performed to within several percent in even very extreme conditions. Moreover, it can be shown that most of the disagreement of their theory with their experiment had to do with assumption (iv). For precise work, to 0.1% or better, assumption (v) needs to be relaxed as well.

The isotropic theory of Kondo and Randolph can be extended to

$$A_{\mathrm{pn}} = \frac{r_0^2}{4\pi V_{\mathrm{cav}}} \int \frac{\mathrm{d}A_1}{r^2} \int \mathrm{d}A_2 \frac{\cos\psi_{21} \cos\psi_{12}}{h} (1 + \omega \cos\Theta) \tag{2}$$

where Θ is the angle between the vector from the point source to $\mathrm{d}A_1$, the incident photon direction, and the vector from $\mathrm{d}A_1$ to $\mathrm{d}A_2$, the direction of the electron through the cavity. The parameter ω is a measure of the degree of anisotropy of the electron distribution. Rather than employ the initial distribution from the Compton or photoelectric interactions, electron multiple scattering must play a role in the electron distributions. Therefore, it is assumed that ω may be determined by the primary equilibrium electron angular distribution in the wall material weighted by the energy deposition. (The spectrum was calculated to be proportional to the stopping power times the track length for an electron being tracked at a given angle.) In principle, ω may be dependent on r_0. However, the assumption made should become increasingly more valid for increasing r_0, by Fano's theorem (Fano 1954). In addition to relaxing assumption (v), assumption (iii) is also relaxed somewhat because an energy-deposition weighted determination will be made for ω so that differential stopping power effects are also included. The appropriate choice for ω is discussed in the next section.

Equation (2) may be written

$$A_{\mathrm{pn}} = A_{\mathrm{pn}}^{\mathrm{KR}} + \omega A'_{\mathrm{pn}} \tag{3}$$

where $A_{\mathrm{pn}}^{\mathrm{KR}}$ is given by Kondo and Randolph's theory expressed in (1) and A'_{pn} is given by

$$A'_{\mathrm{pn}} = \frac{r_0^2}{4\pi V_{\mathrm{cav}}} \int \frac{\mathrm{d}A_1}{r^2} \int \mathrm{d}A_2 \frac{\cos\psi_{21} \cos\psi_{12} \cos\Theta}{h}. \tag{4}$$

Kondo and Randolph reduced the four-dimensional integrations in (1) to an analytic expression for a spherical geometry and for cylindrical and pancake geometries to

a summation of two 1-dimensional integrals which were then integrated numerically. The anisotropic contribution, A'_{pn}, is exactly zero for spheres and may be reduced to a set of 2-dimensional integrations for pancake and cylindrical chambers involving the complete elliptic functions, E_0, F_0 and Π_0. The following equations may be derived by methods similar to those employed by Kondo and Randolph. Summarising the results for A'_{pn}:

For spherical geometries:

$$A'_{pn} = 0. \tag{5}$$

For Farmer-type geometries (cylinders irradiated on the curved side wall (S)):

$$A'_{pn} = A_S^{ss} + A_S^{se} + A_S^{es} + A_S^{ee} \tag{6}$$

separating the contributions for electrons originating on the curved side wall and terminating on the side wall (ss), side wall to flat end wall (se), end wall to side wall (es), and end wall to end wall (ee). These individual contributions are

$$\begin{aligned}
A_S^{ss} &= \int_{-1}^{1} dx \left(G_{1a}(x,\alpha,\sigma) \int_{-1}^{1} dy\, f_{1a}(x,y,\sigma) + G_{1b}(x,\alpha,\sigma) \int_{-1}^{1} dy\, f_{1b}(x,y,\sigma) \right) \\
A_S^{se} &= \int_{-1}^{1} dx \left(G_{1a}(x,\alpha,\sigma) \int_{0}^{1} dy\, f_{2a}(x,y,\sigma) + G_{1b}(x,\alpha,\sigma) \int_{0}^{1} dy\, f_{2b}(x,y,\sigma) \right) \\
A_S^{es} &= \int_{0}^{1} dx \left(G_{2a}(x,\alpha,\sigma) \int_{-1}^{1} dy\, f_{3a}(x,y,\sigma) + G_{2b}(x,\alpha,\sigma) \int_{-1}^{1} dy\, f_{3b}(x,y,\sigma) \right) \\
A_S^{ee} &= \int_{0}^{1} dx \left(G_{2a}(x,\alpha,\sigma) \int_{0}^{1} dy\, f_{4a}(x,y,\sigma) + G_{2b}(x,\alpha,\sigma) \int_{0}^{1} dy\, f_{4b}(x,y,\sigma) \right)
\end{aligned} \tag{7}$$

where

$$\begin{aligned}
G_{1a}(x,\alpha,\sigma) &= \frac{q}{4\alpha^{3/2}} \{ [1 - \tfrac{1}{2}(1+\alpha)q^2] \Pi_0(q^2,q) - F_0(q) \} \\
G_{1b}(x,\alpha,\sigma) &= \frac{q^3}{8\alpha^{\frac{1}{2}}} \Pi_0(q^2,q) \\
G_{2a}(x,\alpha,\sigma) &= \frac{r}{(4\alpha x)^{3/2}} \{ 2[\Pi_0(r^2,r) - F_0(r)] - r(1+\alpha x)\Pi_0(r^2,r) \} \\
G_{2b}(x,\alpha,\sigma) &= \alpha \left(\frac{r^2}{4\alpha x} \right)^{3/2} \Pi_0(r^2,r)
\end{aligned} \tag{8}$$

$$\begin{aligned}
F_0(k) &= \frac{2}{\pi} \int_0^{\pi/2} d\theta\, (1 - k^2 \sin^2\theta)^{-1/2} \\
\Pi_0(k^2,k) &= \frac{2}{\pi} \int_0^{\pi/2} d\theta\, (1 - k^2 \sin^2\theta)^{-3/2} = F_0(k) + \frac{k^2}{1-k^2} E_0(k) \\
E_0(k) &= \frac{2}{\pi} \int_0^{\pi/2} d\theta\, (1 - k^2 \sin^2\theta)^{1/2}
\end{aligned} \tag{9}$$

$$q^2 = 4\alpha[(1+\alpha)^2 + \alpha^2 x^2/\sigma^2]^{-1} \qquad r^2 = 4\alpha x[(1+\alpha x)^2 + \alpha^2/\sigma^2]^{-1} \tag{10}$$

$$f_{1a}(x,y,\sigma) = \frac{1}{8\sigma}\left[1 - \frac{(x-y)^2}{\sigma^2}\left(1 - \frac{|x-y|[5\sigma^2 + (x-y)^2]}{[4\sigma^2 + (x-y)^2]^{3/2}}\right)\right]$$

$$f_{1b}(x,y,\sigma) = \frac{x(y-x)}{8\sigma^3}\left(1 - \frac{|x-y|[6\sigma^2 + (x-y)^2]}{[4\sigma^2 + (x-y)^2]^{3/2}}\right)$$

$$f_{2a}(x,y,\sigma) = \frac{1+x}{8\sigma}$$
$$\times\left(1 - \frac{(1+x)^2 - \sigma^2(1-y)}{\{2\sigma^2[(1+x)^2 + \sigma^2(1-y)] + [(1+x)^2 - \sigma^2(1-y)][(1+x)^2 + \sigma^2(1+y)]\}^{1/2}}\right.$$
$$\left. - \frac{2\sigma^2[(1+x)^2 - \sigma^2(1-y)][(1+x)^2 + \sigma^2(1-y)]}{\{2\sigma^2[(1+x)^2 + \sigma^2(1-y)] + [(1+x)^2 - \sigma^2(1-y)][(1+x)^2 + \sigma^2(1+y)]\}^{3/2}}\right)$$

$$f_{2b}(x,y,\sigma) = -\frac{\sigma x(1+x)^2}{2}$$
$$\times\left(\frac{(1+x)^2 + \sigma^2(1-y)}{\{2\sigma^2[(1+x)^2 + \sigma^2(1-y)] + [(1+x)^2 - \sigma^2(1-y)][(1+x)^2 + \sigma^2(1+y)]\}^{3/2}}\right)$$

$$f_{3a}(x,y,\sigma) = \frac{(1+y)}{4\sigma}\left(1 - \frac{\sigma^2(1-x^2) + (1-y)^2}{\{[\sigma^2(1-x^2)]^2 + 2\sigma^2(1+x^2)(1+y)^2 + (1+y)^4\}^{1/2}}\right.$$
$$\left. - \frac{2\sigma^2x^2[\sigma^2(1-x^2) - (1+y)^2]^2}{\{[\sigma^2(1-x^2)]^2 + 2\sigma^2(1+x^2)(1+y)^2 + (1+y)^4\}^{3/2}}\right)$$

$$f_{3b}(x,y,\sigma) = -\frac{x(1+y)^2}{2\sigma}\left(1 - \frac{1}{\{[\sigma^2(1-x^2)]^2 + 2\sigma^2(1+x^2)(1+y)^2 + (1+y)^4\}^{1/2}}\right.$$
$$\left. + \frac{[\sigma^2(1-x^2) - (1+y)^2][\sigma^2(1+x^2) + (1+y)^2]}{\{[\sigma^2(1-x^2)]^2 + 2\sigma^2(1+x^2)(1+y)^2 + (1+y)^4\}^{3/2}}\right)$$

$$f_{4a}(x,y,\sigma) = 2\sigma^3x^2[\sigma^2(x^2-y) + 4]\left\{16\sigma^2x^2 + [4 + \sigma^2(y-x^2)]^2\right\}^{-3/2}$$

$$f_{4b}(x,y,\sigma) = -4\sigma x[\sigma^2(x^2+y) + 4]\left\{16\sigma^2x^2 + [4 + \sigma^2(y-x^2)]^2\right\}^{-3/2}. \tag{11}$$

The above equations are written using the dimensionless quantities

$$\sigma = a/L \qquad \alpha = a/r_0 \tag{12}$$

where a is the cavity radius, L is the half-length of the cavity, and r_0 is the distance from the point source to the centre of the cavity. A detailed derivation of A_S^{ss} is given in the appendix.

For pancake geometries (cylinders irradiated on the flat end wall (E)), similar expressions result with the form

$$A'_{\mathrm{pn}} = A_{\mathrm{E}}^{\mathrm{ss}} + A_{\mathrm{E}}^{\mathrm{se}} + A_{\mathrm{E}}^{\mathrm{es}} + A_{\mathrm{E}}^{\mathrm{ee}} \tag{13}$$

where

$$\begin{aligned}
A_{\mathrm{E}}^{\mathrm{ss}} &= \int_{-1}^{1} \mathrm{d}x \left(G_{3\mathrm{a}}(x,\lambda,\sigma) \int_{-1}^{1} \mathrm{d}y\ f_{1\mathrm{a}}(x,y,\sigma) + G_{3\mathrm{b}}(x,\lambda,\sigma) \int_{-1}^{1} \mathrm{d}y\ f_{1\mathrm{b}}(x,y,\sigma) \right) \\
A_{\mathrm{E}}^{\mathrm{se}} &= \int_{-1}^{1} \mathrm{d}x \left(G_{3\mathrm{a}}(x,\lambda,\sigma) \int_{0}^{1} \mathrm{d}y\ f_{2\mathrm{a}}(x,y,\sigma) + G_{3\mathrm{b}}(x,\lambda,\sigma) \int_{0}^{1} \mathrm{d}y\ f_{2\mathrm{b}}(x,y,\sigma) \right) \\
A_{\mathrm{E}}^{\mathrm{es}} &= \int_{0}^{1} \mathrm{d}x \left(G_{4\mathrm{a}}(x,\lambda,\sigma) \int_{-1}^{1} \mathrm{d}y\ f_{3\mathrm{a}}(x,y,\sigma) + G_{4\mathrm{b}}(x,\lambda,\sigma) \int_{-1}^{1} \mathrm{d}y\ f_{3\mathrm{b}}(x,y,\sigma) \right) \\
A_{\mathrm{E}}^{\mathrm{ee}} &= \int_{0}^{1} \mathrm{d}x \left(G_{4\mathrm{a}}(x,\lambda,\sigma) \int_{0}^{1} \mathrm{d}y\ f_{4\mathrm{a}}(x,y,\sigma) + G_{4\mathrm{b}}(x,\lambda,\sigma) \int_{0}^{1} \mathrm{d}y\ f_{4\mathrm{b}}(x,y,\sigma) \right)
\end{aligned} \tag{14}$$

and

$$\begin{aligned}
G_{3\mathrm{a}}(x,\lambda,\sigma) &= -\frac{\sigma\lambda}{2} \left(\frac{1-\lambda x}{[(1-\lambda x)^2 + \lambda^2 x^2]^{3/2}} + \frac{1+\lambda x}{[(1+\lambda x)^2 + \lambda^2 x^2]^{3/2}} \right) \\
G_{3\mathrm{b}}(x,\lambda,\sigma) &= -\frac{\sigma}{2x} \left(\frac{1-\lambda x}{[(1-\lambda x)^2 + \lambda^2 x^2]^{3/2}} - \frac{1+\lambda x}{[(1+\lambda x)^2 + \lambda^2 x^2]^{3/2}} \right) \\
G_{4\mathrm{a}}(x,\lambda,\sigma) &= -\frac{\sigma\lambda x}{2} \left(\frac{1-\lambda}{[(1-\lambda)^2 + \lambda^2\sigma^2 x^2]^{3/2}} + \frac{1+\lambda}{[(1+\lambda)^2 + \lambda^2\sigma^2 x^2]^{3/2}} \right) \\
G_{4\mathrm{b}}(x,\lambda,\sigma) &= -\frac{\sigma}{2} \left(\frac{1-\lambda}{[(1-\lambda)^2 + \lambda^2\sigma^2 x^2]^{3/2}} - \frac{1+\lambda}{[(1+\lambda)^2 + \lambda^2\sigma^2 x^2]^{3/2}} \right)
\end{aligned} \tag{15}$$

where another dimensionless quantity is used,

$$\lambda = L/r_0. \tag{16}$$

Note that, similar to the analysis by Kondo and Randolph, the source dependence of A'_{pn} is contained entirely by the G factors, while the f factors only depend on the chamber shape and are identical for both orientations of the cylindrical chamber.

More relevant for this study is the behaviour of the A'_{pn}s for practical measurement distances. For the cylindrical chamber in either orientation, in the limit that $L, R \ll r_0$

$$\lim_{L,R \ll r_0} A_{\mathrm{pn}} \longrightarrow 1 + \omega\kappa'_{(\mathrm{E})}^{(\mathrm{S})}(R/r_0) + \kappa_{(\mathrm{E})}^{\mathrm{KR}(\mathrm{S})}(R/r_0)^2 + \ldots \tag{17}$$

where unity and the second-order terms, $\kappa_{(\mathrm{E})}^{\mathrm{KR}(\mathrm{S})}$, come entirely from Kondo and Randolph's theory and the first-order terms, $\kappa'_{(\mathrm{E})}^{(\mathrm{S})}$, come entirely from the anisotropic portion of the electron distribution. For the Farmer-type geometry the expression for κ' is

$$\begin{aligned}
\kappa'_{\mathrm{S}} = \frac{1}{2} \Bigg[& \int_{-1}^{1} \mathrm{d}x \left(\int_{-1}^{1} \mathrm{d}y [f_{1\mathrm{a}}(x,y,\sigma) + f_{1\mathrm{b}}(x,y,\sigma)] + \int_{0}^{1} \mathrm{d}y [f_{2\mathrm{a}}(x,y,\sigma) + f_{2\mathrm{b}}(x,y,\sigma)] \right) \\
& + \int_{0}^{1} \mathrm{d}x \left(\int_{-1}^{1} \mathrm{d}y [f_{3\mathrm{a}}(x,y,\sigma) + f_{3\mathrm{b}}(x,y,\sigma)] + \int_{0}^{1} \mathrm{d}y [f_{4\mathrm{a}}(x,y,\sigma) + f_{4\mathrm{b}}(x,y,\sigma)] \right) \Bigg]
\end{aligned} \tag{18}$$

while for the pancake geometry

$$\kappa'_E = -2\kappa'_S. \tag{19}$$

For the spherical chamber

$$\lim_{L,R \ll r_0} A_{pn} \longrightarrow 1 + \tfrac{1}{3}(R/r_0)^2 \tag{20}$$

where the $\frac{1}{3}$ factor comes from Kondo and Randolph's theory. The first and second order factors, κ'_S, κ'_E, κ_S^{KR}, and κ_E^{KR} are plotted in figure 1 for reasonable values of $\sigma = L/R$. For practical measurements, the range covered should apply to any chamber and, if the chamber is not too close to the source, the asymptotic expressions given in (17)–(19) hold, and one may quickly determine the A_{pn} correction. Note that the κ' terms vanish when $\sigma = 1.12$ which is close to unity where the cylinder approaches the shape of a sphere. In the same vicinity, the second order factors are close to $\frac{1}{3}$, the spherical value.

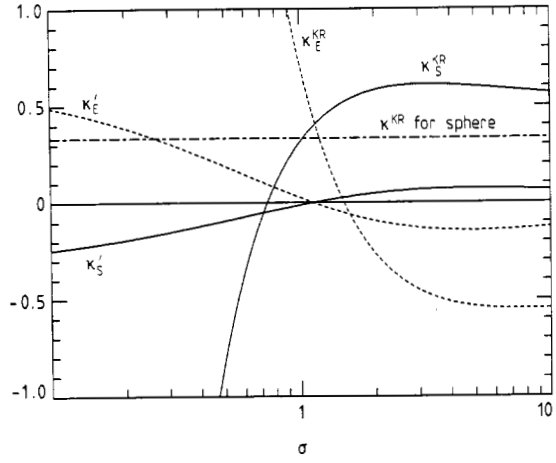

Figure 1. First and second order κ-factors for the large distance limit of A_{pn}.

2.1. Determination of ω

The ω-parameter is a measure of the anisotropy of the electron distribution. Consider figure 2, which depicts a Monte Carlo calculation of the energy-deposition weighted primary electron distribution above 10 keV in graphite (δ-rays are included, Δ = 10 keV). The electrons were set in motion by monoenergetic 1.25 MeV photons and the effects of photon attenuation were removed, because attenuation is accounted for by the A_{at} correction factor (Bielajew 1986, 1990). (Other details of the Monte Carlo calculations are given in § 3.) The probability distribution, $P(\cos\theta)$, is differential in $\cos\theta$ and normalised so that

$$\int_{-1}^{1} \mathrm{d}(\cos\theta)\ [\mathrm{d}P(\cos\theta)/\mathrm{d}(\cos\theta)] = 2. \tag{21}$$

The Kondo and Randolph isotropy assumption is represented by the constant line at unity. The anisotropy approximation, $1+\omega\cos\theta$, is a first order expansion in Legendre polynomials. Therefore, ω was obtained from the Monte Carlo data by the integral

$$\omega = \frac{3}{2}\int_{-1}^{1} \mathrm{d}(\cos\theta)\ \cos\theta[\mathrm{d}P/\mathrm{d}(\cos\theta)]_{\substack{\text{Monte}\\\text{Carlo}}}. \tag{22}$$

It is clear, at least for this example, that the Kondo and Randolph isotropy assumption is an over-simplification. The simple anisotropy assumption, $1+\omega\cos\theta$, fits the Monte Carlo better but a closer fit would require more terms in a Legendre series. Fortunately, the inclusion of just one term seems to work well for the calculation of A_{pn} for the cases studied. For 1.25 MeV photons, $\omega = 1.055 \pm 0.006(1\sigma)$. Although values of ω such that $|\omega| > 1$ are unphysical (the electron distributions can be negative!), one can accept this as part of the over-simplification of the first-order modelling of the electron distribution.

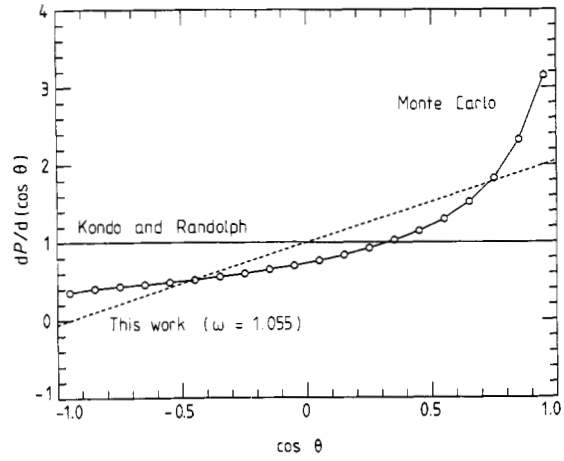

Figure 2. The energy-deposition weighted angular distribution of primary electrons (δ-rays included) above 10 keV for 1.25 MeV incident photons.

The dependence of ω with incident photon energy is given in figure 3 for the energy-deposition weighted primary electron distribution above a 10 keV cutoff in graphite. The maximum energy shown is for 1.25 MeV incident photons. As the incident energy is reduced, one sees a slow decrease in ω as increased multiple scattering causes the electron distribution to become more isotropic. However, a local minimum of about 0.95 occurs in the vicinity of 500 keV. Below this there is a sharp peak at around 85 keV. The explanation for this behaviour is that by employing energy weighting and restricting the contribution to electrons above the cutoff energy, the average Compton electron recoil angle for contributing electrons decreases as the incident photon energy is decreased. At a limit of about 55 keV incident photon energy, the only Compton electrons contributing are just above threshold and directed in the forward direction. Below this threshold, no Compton electrons contribute and the distribution is determined by the photoelectron distribution. The values for ω that would be obtained by using purely Compton or photoelectrons without multiple scattering are also shown in figure 3. (The unbound Compton distribution was taken

from Nelms (1953) while the photoelectron distribution is from the theory of Sauter (1931). Sauter's theory was also employed to model the photoelectron angle in the Monte Carlo calculations (Bielajew and Rogers 1986).) Thus, the location of the peak is determined by the cutoff energy. At low incident energies approaching the cutoff energy, the use of the present theory is inappropriate since it neglects the electrons generated in the cavity gas. At higher energies, well above the cutoff, the values of ω are more realistic and only weakly dependent on the cutoff energy.

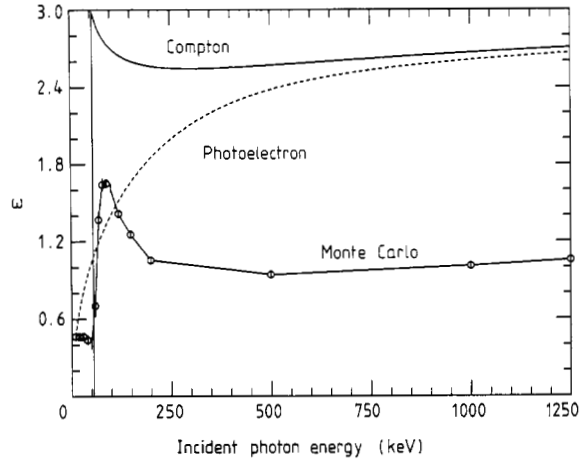

Figure 3. Values of ω against incident photon energy for the energy-deposition weighted electron distributions (δ-rays included) above 10 keV. ω-values for theoretical distributions Compton and photoelectron angular distributions are shown as well.

Therefore, the appropriate value of ω also depends indirectly on the size of the cavity through the parameter Δ of Spencer–Attix cavity theory (Spencer and Attix 1955). Electrons below this energy in a cavity should be considered to have been generated there through knock-on electron interactions. Recall that a basic assumption of the analytic theories was that electrons that deposit dose in the cavity are generated in the walls of the cavity. Therefore, only the electrons above Δ should be considered. Large cavities, where an appreciable part of the dose to the cavity comes from primary photon interactions within the cavity gas, are beyond the scope of the present theory. A plot of ω versus Δ in graphite is given in figure 4 for a monoenergetic incident energy of 1.25 MeV for a range of Δ covering almost any small chamber. The variation in ω is monotonic from about 0.88 to 1.15 for Δ ranging from 1 to 25 keV. Smaller values of ω are obtained for smaller values of Δ since more energy is deposited from more isotropically distributed δ-rays. For a typical ^{60}Co incident photon spectrum (Rogers *et al* 1988), ω was calculated to be 1.058 ± 0.0011, and for a typical ^{137}Cs spectrum (Costrell 1962) the value 0.975 ± 0.006 was obtained. Having determined the size of one's chamber in terms of Δ, one should use the ω-value from figure 4 in conjunction with the appropriate expressions from the previous section or the κ-factors depicted in figure 1.

3. Monte Carlo comparisons

In this section Monte Carlo calculations of ion chamber response and correction factors

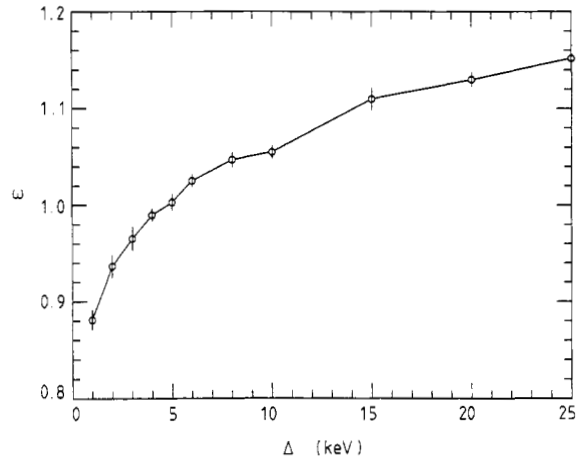

Figure 4. Values of ω for 1.25 MeV incident photons against Δ.

are described and the calculations to obtain the energy-deposition weighted primary electron distributions in § 2.1 are outlined. The EGS4 code system (Nelson *et al* 1985) is employed along with the PRESTA electron transport algorithm (Bielajew and Rogers 1987) that has been shown to calculate absolute ion chamber response reliably for carbon-walled chambers. For the ω anisotropy parameter, it was found necessary to employ an additional restriction on electron step-size whereby the maximum amount of energy lost to 'continuous' processes for each electron step was restricted to 2.0%. (ESTEPE was set to 0.02 (Rogers 1984).) Because PRESTA can take large electron steps, the additional restriction was found necessary to sample the angular distributions smoothly.

The EGS4 user codes employed in this report, DISTRZ (electron angular distributions, cylindrical-planar geometry) CAVRZ (cylindrical-planar geometry) and CAVSPH (spherical-conical geometry), are offspring of CAVITY, which has been used previously to calculate scatter and attenuation correction factors (Bielajew *et al* 1985, Rogers *et al* 1985). The reliability of the Monte Carlo calculations is considered to be within the stated uncertainties, which were estimated by dividing each calculation into 10 batches and calculating the estimated variance of the mean. For the angular distribution simulations, 10^4–10^5 primary photon interactions were used for each simulation which was performed on a μVAX 3600. Typical simulation times were 1–30 CPU minutes per incident photon energy. For the cavity chamber simulations, a minimum of about 8×10^5 primary photon interactions were employed for each simulation although as many as 9×10^6 were used for some cases. The cavity chamber simulations were performed on an IBM 3090 and typical simulation times were 1–7 h CPU per chamber for each distance. For both types of calculations, the primary photon was 'forced' to interact at least once in the chamber (a standard 'variance reduction' technique, see, for example, Rogers and Bielajew (1984)).

The angular distribution calculations were performed in a cylindrical-planar geometry. The medium was uniform 1.70 g cm^{-3} graphite, and the energy-deposition weighted angular distributions from electrons set in motion from the primary interactions as well as δ-rays set in motion by these electrons were scored. The electron transport threshold, below which no electron is transported, was set to Δ, the δ-ray creation threshold. (In

the terminology of the EGS4 code (Nelson *et al* 1985), ECUT-RM=AE-RM=Δ(MeV), RM is the rest mass energy of the electron.) The photon creation threshold was set to 1 keV (AP=0.001). This is small enough so that the radiative part of the electron stopping power and any effects of subthreshold photon generation can be ignored. The size of the cylindrical scoring region was 1 cm in depth by 1 cm in diameter which was surrounded by 0.3 cm walls to enable the development of full build-up. The broad, parallel beam of photons impinged normally upon one of the flat sides. The primary electron fluence was 'unweighted' by the average photon attenuation (Bielajew 1986, 1990), compensating for primary photon attenuation thereby producing a true charged particle equilibrium in the scoring region.

The cavity calculations were performed in pancake (planar geometry), Farmer-type (cylindrical), and spherical chambers with graphite walls and air-density (1.205×10^{-3} g cm^{-3}) graphite gas in the cavity. The employment of graphite gas eliminates any possible mass stopping power effects and fluence correction effects, as evident from equations (15) and (16) of Bielajew (1990) along with the application of Fano's (1954) theorem. (The density effect was not included so that the mass stopping powers were identical for both the wall material and the cavity gas.)

The response, R, is defined as the dose to the cavity corrected for scatter and attenuation (Bielajew 1986, 1990) and normalised per unit incident photon fluence at r_0. The incident photons were monoenergetic at 1.25 MeV. Then, the ratio $(R(r_0)/A_{\rm pn}(r_0))/R(\infty)$ is plotted against r_0^{-1}, where $R(\infty)$ is defined as the chamber response at infinite source to chamber distance and $A_{\rm pn}(r_0)$ is the Monte Carlo result as calculated by (17) of Bielajew (1990). (A broad parallel beam was used to simulate this case.) The quantity $r_0(A_{\rm pn}-1)$ is also plotted against r_0^{-1} and the Monte Carlo calculations are compared with the predictions of the Kondo and Randolph (1960) theory and the anisotropic theory developed in this work.

If the point source non-uniformity correction is being applied properly, then the ratio $(R/A_{\rm pn})/R(\infty)$ should be a constant and not depend on r_0. This was demonstrated for large chambers in extreme conditions in a previous paper (Bielajew 1990). The Kondo and Randolph theory predicts

$$\lim_{L,R\ll r_0} r_0(A_{\rm pn}-1) \longrightarrow \kappa^{\rm KR} R(R/r_0) \tag{23}$$

which goes to zero in the limit as $r_0^{-1} \longrightarrow 0$. The theory proposed in this work predicts

$$\lim_{L,R\ll r_0} r_0(A_{\rm pn}-1) \longrightarrow \omega\kappa' R \tag{24}$$

which has a non-zero limit. The Monte Carlo calculations were used to decide between the two analytic theories.

Finally, in § 3.4, the point source non-uniformity correction factors are calculated for various chambers used by Standards laboratories for absolute air kerma or exposure standards.

3.1. Spherical chambers

A spherical chamber was employed in this study having a cavity region 2 cm in diameter with 0.273 cm thick 1.83 g cm^{-3} graphite walls. No electrode was modelled. The Monte Carlo response corrected by Monte Carlo calculated $A_{\rm wall}$ and $A_{\rm pn}$ perturbations (Bielajew 1990) is plotted in figure 5. The $A_{\rm wall}$ correction factors did not vary by more

than (0.4±0.2)% over all distances. To within the estimated statistics which varied from 0.2% to 0.5%, the corrected responses show no residual source distance dependence despite corrections by A_{pn} as large as about 30%. The plot of Monte Carlo calculated $r_0(A_{pn}-1)$ against r_0^{-1} is given in figure 6 and compared with the theory of Kondo and Randolph (1960). The anisotropic theory developed herein provides the identical correction for spherical chambers. The agreement between Monte Carlo and theory is excellent in this case. For practical measurements, with distances of the order of a metre or so, there is no correction for this chamber.

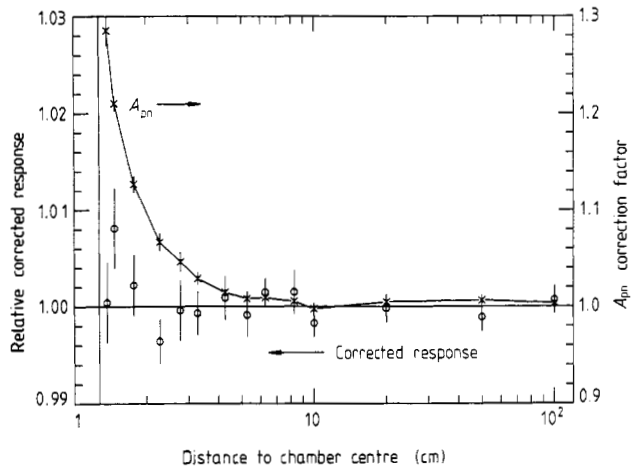

Figure 5. The Monte Carlo response to monoenergetic 1.25 MeV photons of the spherical chamber corrected by A_{wall} and the point source non-uniformity correction, A_{pn}. The vertical line at 1.273 cm is the outer radius of the spherical chamber. Graphite sphere, 2.0 cm diameter.

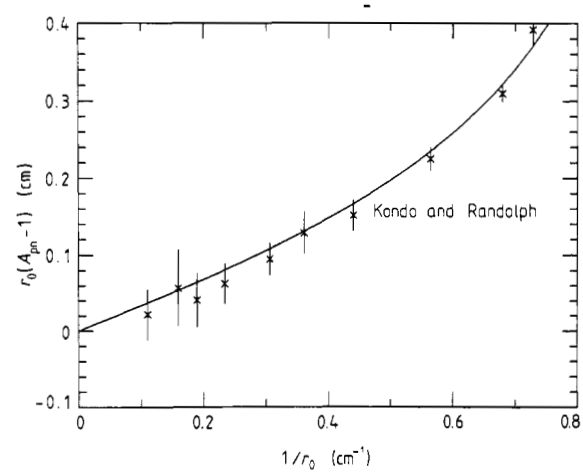

Figure 6. A comparison of the Monte Carlo calculated A_{pn} for monoenergetic 1.25 MeV photons (×) with the theory of Kondo and Randolph for the spherical chamber. The anisotropic theory presented in this report predicts the identical curve to Kondo and Randolph's isotropic theory for spherical geometries. The error bars are 1σ estimates of the Monte Carlo calculations. Graphite sphere, 2.0 cm diameter.

3.2. Pancake chambers

The chamber employed in this study had a cavity region 2 cm in diameter, 2 mm in depth, with 0.273 cm thick 1.83 g cm^{-3} graphite walls. Neither an electrode nor a guard region was modelled with this chamber. The Monte Carlo response corrected by Monte Carlo calculated A_{wall} and A_{pn} perturbations is plotted in figure 7. The A_{wall} correction factors varied by (1.7±0.3)% over the distances calculated. For distances greater than 1 cm, the corrected responses show no residual source distance dependence within the estimated statistics which varied from 0.2% to 0.5% despite corrections by A_{pn} as large as about 70%. For source distances less than 1 cm from the cavity centre there appears to be a systematic departure to a level of about 0.5%. This is certainly due to simplifying approximations in the Monte Carlo calculation of A_{pn} which can cause the correction to be too large to order $(r_e/r_0)^2$. (The approximation to the Monte Carlo calculations is described by Bielajew (1990).) Since this report is concerned primarily with the large distance behaviour and the deviation is in the right direction with the right order of magnitude, this difference was not investigated further. This departure was only observed for the pancake chamber where the closest approach to the point source was possible.

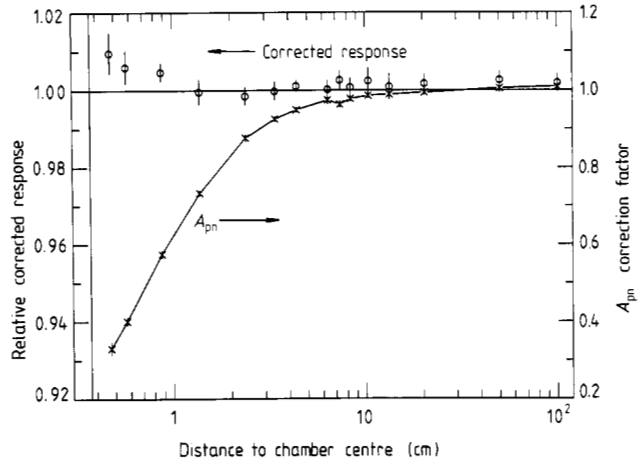

Figure 7. The Monte Carlo response to monoenergetic 1.25 MeV photons of the pancake chamber corrected by A_{wall} and the point source non-uniformity correction, A_{pn}. The vertical line at 0.373 cm is the outer edge of the flat face of the pancake chamber. Graphite pancake, 2 cm diameter, 2 mm depth.

The plot of Monte Carlo calculated $r_0(A_{pn} - 1)$ against r_0^{-1} is given in figure 8 and compared with the predictions of the analytic theories. In this comparison, the anisotropic theory agrees much better than the theory by Kondo and Randolph at all distances. For this chamber, a value of 1.04 was chosen for ω corresponding to a Δ of 6 keV from figure 4. For practical measurements, with distances of the order of a metre or so, the correction for this chamber is of the order of 0.13%. This may also have been determined from (17) and figure 1 ($\sigma = 10$ for this chamber) which suggests that the leading asymptotic behaviour for A_{pn} is $1 + 0.13/r_0$, with r_0 measured in cm for r_0 greater than 3 cm or so.

3.3. Farmer-type chambers

In this study a cylindrical chamber was modelled having a cavity region 1 cm in

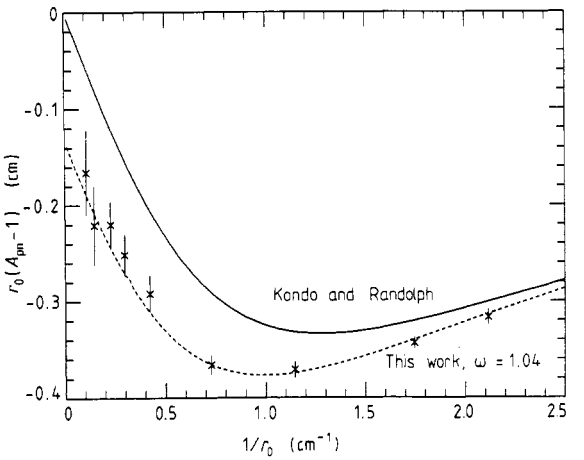

Figure 8. A comparison of the Monte Carlo calculated A_{pn} for monoenergetic 1.25 MeV photons (×) with the theory of Kondo and Randolph (fulll curve) and the anisotropic theory presented in this report (broken curve). The error bars are 1σ estimates of the Monte Carlo calculations. Graphite pancake, 2 cm diameter, 2 mm depth.

diameter, 2 cm in depth, an electrode 4 mm in diameter, with 0.273 cm thick 1.83 g cm^{-3} graphite walls. The Monte Carlo response corrected by Monte Carlo calculated A_{wall} and A_{pn} perturbations is plotted in figure 9. The A_{wall} correction factors varied by (0.7±0.2)% over the distances calculated. The corrected responses show no residual source distance dependence within the estimated statistics which varied from 0.2% to 0.6% despite corrections by A_{pn} as large as about 20%. The plot of Monte Carlo calculated $r_0(A_{pn}-1)$ against r_0^{-1} is given in figure 10 and compared with the predictions of the analytic theories. In this comparison, the anisotropic theory agrees much better than the theory by Kondo and Randolph at all distances. The slight departure at large distances is probably due, in this case, to not considering the effects of the electrode in the analytic theory. If this is true, then the effect appears to be no more than 0.03% at 1 m. For this chamber, a value of 1.12 was chosen for ω corresponding to a Δ of 15 keV from figure 4. For practical measurements, with distances of the order of a metre or so, the correction for this chamber is of the order of 0.05%. This may also have been determined from (17) and figure 1 ($\sigma = 0.5$ for this chamber) which suggests that the leading asymptotic behaviour for A_{pn} is $1 + 0.05/r_0$, with r_0 measured in cm for r_0 greater than 3 cm or so.

4. Application to standard chambers

The point source non-uniformity correction factors are calculated for the standard chambers of the BIPM, NIST(NBS), NRCC, PTB, ENEA (Comitato Nazionale per la Ricerca e per lo Sviluppo dell'Energia Nucleare e delle Energie Alternative, Italy) and IRD (Instituto de Radioproteçao e Dosimetria, Brazil). Details about the geometry of these chambers is available in the literature (Niatel *et al* 1975, Loftus and Weaver 1974, Shortt and Ross 1986, Laitano and Toni 1983, de Almeida and Niatel 1986). The comparison is complicated owing to the fact that the radial correction factor k_{rn} used by Standards laboratories accounts not only for the point-source $1/r^2$ fall-off in the

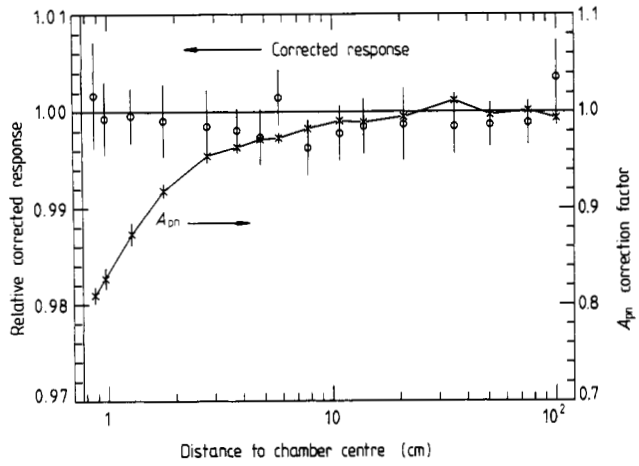

Figure 9. The Monte Carlo response to monoenergetic 1.25 MeV photons of the Farmer-type chamber corrected by A_{wall} and the point source non-uniformity correction, A_{pn}. The vertical line at 0.773 cm is the outer radius of the flat face of the Farmer-type chamber. Graphic chamber, 1 cm diameter, 2 cm length.

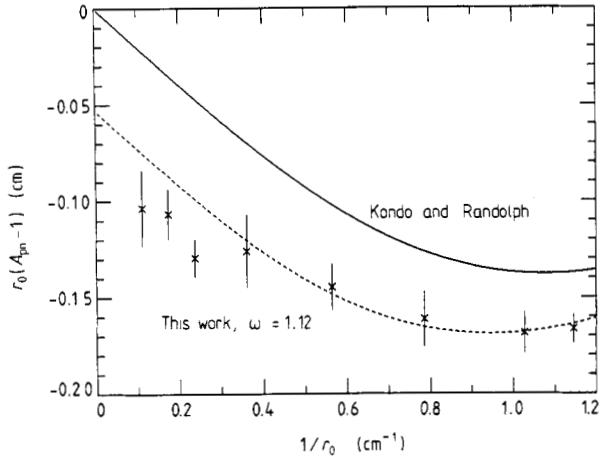

Figure 10. A comparison of the Monte Carlo calculated A_{pn} for monoenergetic 1.25 MeV photons (×) with the theory of Kondo and Randolph (full curve) and the anisotropic theory presented in this report (broken curve). The error bars are 1σ estimates of the Monte Carlo calculations.

lateral direction, but also for finite-size source effects, room, air and collimator scatter. Although a measurement of the size of this perturbation (Boutillon and Niatel 1973) is consistent with it arising entirely from $1/r^2$ fall-off, the precision of the measurement does not rule out contributions from finite-source effects, air, room and collimator scatter. Therefore, the comparison of $k_{pn} = A_{pn}^{-1}$ is probably more properly done with the product of $k_{an}k_{rn}$, although both the k_{an} and k_{rn} factors, as currently employed by the Standards laboratories, are presented separately below. Certainly k_{pn} contains all of k_{an} and a portion of k_{rn}. If k_{pn} is to be adopted, then experimental derivations of k_{rn} may have to be re-interpreted to take out the point-source lateral fall-off. The results are summarised in table 1. The source-to-detector distance of 112.01 cm was used in some of the calculations since this was the distance used in the intercomparison by

Niatel *et al* (1975) and by de Almeida and Niatel (1986). The distance of 97 cm for the NRCC chamber is their standard calibration distance (Shortt and Ross 1986) and the distance of 111 cm is the standard calibration distance for the ENEA (Laitano and Toni 1983). The 0.1% estimate of the error in k_{pn} is based on the uncertainty in the choice of ω, over-simplification of the theoretical model either due to the neglect of electrodes, guard areas, or the way the anisotropy was modelled. A uniform value of $\omega = 1.1$ was chosen for all the chambers. As seen in § 2.1, the dependence of ω on chamber size is quite weak and this choice should suit all the chambers to within the stated uncertainty in k_{pn} which is directly proportional to the value of ω.

Table 1. A comparison of the point source non-uniformity correction factor, k_{pn}, calculated from the anisotropic theory, with k_{an} and k_{rn} for chambers from various Standards laboratories. Except for k_{pn}, all other data are taken from Niatel *et al* (1975), Laitano and Toni 1983, de Almeida and Niatel 1986 and Shortt and Ross (1986).

Laboratory	Chamber type	Distance to centre (cm)	Cavity diameter/ height (cm)	k_{an} in use	k_{rn} in use	k_{pn} this work
BIPM	Pancake	112.01	4.50/0.51	0.9968(20)†	1.0013(05)	1.0031(10)
NIST(NBS)-1cc	Sphere	112.01	1.27	1.0000(10)	1.0005(03)	1.0001(10)
NRCC	Cylinder	97.0	1.58/1.61	1.0000(20)	1.0000(02)	1.0001(10)
PTB(a)	Cylinder	112.01	0.6/2.0	0.9955(15)	1.0006(03)	1.0005(10)
PTB(b)	Cylinder	112.01	1.0/2.0	0.9925(15)	1.0006(03)	1.0005(10)
PTB(c)	Pancake	112.01	4.4/0.45	0.9933(15)	1.0014(05)	1.0030(10)
ENEA	Cylinder	111.	1.1/1.1	0.9970(10)	1.0000(10)	1.0001(10)
IRD	Cylinder	112.01	1.1/1.1	1.0000(07)	1.0000(02)	1.0001(10)

†Figures in parentheses are uncertainties in the last figures.

5. Discussion and conclusions

The results of this report are summarised by (17) and (20) and figures 1 and 4. Given a thick-walled ionisation chamber, either spherical or cylindrical in shape, the correction for the non-uniformity of an incident point-source photon field across the chamber can be accounted for. For practical measurements employing chambers at most a few centimetres across a metre or more from the source, a simple formula and a look up chart may be used. For more extreme cases, the more complicated formulae of § 2 or Monte Carlo calculations may be used.

For practical measurements, the correction for spherical chambers is negligible. For practical measurements employing typical Farmer-type chambers, where the depth and diameter are of the same order, the correction is very small, less than 0.1% in the cases studied. For pancake chambers, typically a few centimetres across but only millimetres thick, the corrections for practical measurements can be significant, of the order of 0.3% in some of the cases studied.

This report attempts to resolve two conflicting views. The first opinion, which results in no correction for practical measurements, was most eloquently expressed by Burlin (1959) who stated, '...the electrons will have the geometric attenuation of the photons superimposed on them...'. This statement can be interpreted as follows: Owing to the geometric attenuation ($1/r^2$ fall-off), the increased ionisation in the upstream portion of a chamber is offset by the decreased ionisation in the downstream portion

resulting in a point of measurement which is essentially the centre of the cavity. The second opinion is that adopted by Boutillon and Niatel (1973) who calculate the axial correction factor based on the interaction point of the incident photon in the chamber (somewhat upstream of the geometric centre of the chamber) and the electron deposition function that would arise if the photon beam were not skewed due to the point source distribution (Boutillon 1988). This method leads to a significant correction of $k_{an} = 0.9968 \pm 0.0020$, which can be interpreted as a shift of the point of measurement in the upstream of the centre of the cavity by 1.8 mm.

The explanation as to why neither view is strictly correct is best accomplished by considering a less approximate form for A_{pn} that is obtained by generalising (2)

$$A_{pn} = \frac{r_0^2}{4\pi V_{cav}} \int \frac{dA_1}{r^2} \int dA_2 \frac{\cos\psi_{21} \cos\psi_{12}}{h} f(\cos\Theta) \tag{25}$$

where $f(\cos\Theta)$ is the generalised energy-weighted angular distribution of primary electrons. This distribution may have any form except that is it properly normalised so that A_{pn} is unity when $r_0 \longrightarrow \infty$. One may perform an expansion in $1/r_0$ to obtain the following first-order expression:

$$\lim_{r_0 \longrightarrow \infty} A_{pn} \longrightarrow$$
$$1 - \frac{1}{4\pi V_{cav} r_0} \int dA_1 \int dA_2 \cos\psi_{21} \cos\psi_{12} [2\cos\Theta_0 f(\cos\Theta_0) - \sin^2\Theta_0 f'(\cos\Theta_0)]. \tag{26}$$

The distribution angle, Θ_0, is the angle the electron makes with respect to the fixed direction from the source to the symmetry point of the cavity. (The derivation of (26) assumes that there exists a symmetry point in the cavity whereby any vector from this point to the cavity surface remains on the surface if its sign is changed. This is the case for spheres and cylinders as well as some other symmetric geometries. For asymmetric geometries, one may use (26) to determine the effective centre of the chamber.) The first part of the integrand, $2\cos\Theta_0 f(\cos\Theta_0)$, arises from the change in the photon source strength for different parts of the cavity surface where the electrons are set in motion. For a forward directed beam, this factor leads to a point of measurement upstream of the cavity centre. The second part of the integrand, $\sin^2\Theta_0 f'(\cos\Theta_0)$, accounts for the effect of the rotation of the electron distribution in the direction of the photon beam at the point at which the electron is set in motion. This term accounts for the loss of ionisation in the cavity because the electron paths can be rotated into the chambers walls. The resultant path length shortening and loss of ionisation can be interpreted as the point of measurement being moved further downstream. For isotropic electron distributions (Kondo and Randolph's theory), both parts vanish. In fact, both terms vanish for all distributions even in $\cos\Theta$, that is, those electron distributions that exhibit front-to-back symmetry. (In this case, both upstream and downstream surface elements contribute equally and electron paths that are lost through rotation into the cavity walls are replaced by equal strength ones rotated out of the cavity walls.) The first-order correction also vanishes for spherical chambers employing the $1 + \omega\cos\Theta$ distributions. In one other important case, where the electrons are set off in the same direction as the incident photon that set them in motion, the first-order correction also vanishes. This is seen from the integrand of (26) for which both terms may be collected into a single term, $d[1 - \cos^2\Theta_0 f(\cos\Theta_0)]/d[\cos\Theta_0]$. For a straight-ahead electron distribution, $f(\cos\Theta_0) = 4\pi h^2 \delta(1 - \cos\Theta_0)$ and the first-order integral vanishes.

Thus, Burlin's compelling intuitive argument is valid in this case owing to an exact cancellation of the upstream and downstream effects. It is really the lateral parts of the electron distribution that cause the appearance of the first-order term in cylindrical and pancake geometries.

For cylindrical and pancake geometries, the terms in the integrand of (26) will not cancel implying that significant corrections may be needed for practical measurement distances. Recall the first-order factor κ'_E from figure 1. For small radius pancake chambers ($R/L < 1.12$), the correction places the point of measurement upstream. This comes from the first part of (26). For larger radius chambers, the effect of the skewness of the beam becomes important and the point of measurement effectively moves downstream. The error in the BIPM calculation resulted from the fact that the electron distributions employed were one-dimensional and therefore could not model the second part of the integrand of (26). This ultimately resulted in a correction that departed in the wrong way from unity.

The implications for some of the Standards laboratories are quite large. For example, the results indicate that the BIPM exposure standard should change by about +0.50% while the changes for the PTB chambers range from +0.44% to +0.83%. It would be inappropriate to suggest changes of these magnitudes without further experimental evidence, irrespective of how impressive the agreement is between Monte Carlo and theory. The theory does provide clues as to how such an experiment could be done. One could make use of (19), that is, $\kappa'_E = -2\kappa'_S$ and (17). In other words, the two different orientations of a cylindrical chamber have different magnitudes and *signs* of correction. If one had a cylindrical chamber and made two measurements, one from the curved side M_S and one from the flat side, M_E, then to first order

$$\varepsilon \equiv \frac{M_S - M_E}{M_S + M_E} \approx \frac{3}{2}\omega\kappa'_S\left(\frac{R}{r_0}\right). \tag{27}$$

The measurements must be corrected for differential wall correction factors. These are easily calculated by Monte Carlo methods (Bielajew 1986, 1990). From figure 1 a choice of $\sigma = R/L = 5$ gives $\kappa'_S = 0.07$. Then, with $\omega = 1.1$ and for a typical measurement $R = 2$ cm and $r_0 = 100$ cm, $\varepsilon = 0.0023$. A precision considerably smaller than 0.23% can be achieved experimentally. Similarly, a measurement with another chamber with $\sigma \approx 1$ would give a null result. The essential difficulty in the experiment is the alignment of the chamber so that it is known to rotate about its cavity centre. Alignment in one plane could be accomplished by equalising the chamber response to a 180° rotation. Precise alignment in another plane could be accomplished by using a second source, preferably at 90° with respect to the first one.

Acknowledgments

The author wishes to express his appreciation to his colleagues Dr Carl K Ross and Dr David W O Rogers for their numerous suggestions and critical reviews of this manuscript.

Appendix. Derivation of A_S^{ss}

In this section the derivation of A_S^{ss} is given in detail. The other correction factors may be derived in a similar fashion.

Let the source be at coordinates $(0, r_0, 0)$ and the centre of the chamber be at the origin so that the vector from the point source to the centre of the chamber is, $\boldsymbol{r}_0 = -r_0\hat{\boldsymbol{y}}$, where $\hat{\boldsymbol{y}}$ is the unit vector in the y-direction. Let $\boldsymbol{h}_{1\to2}$ be the vector from $dA_1 = ad\theta_1 dz_1$, where the electron enters the cavity, to $dA_2 = ad\theta_2 dz_2$, where it terminates. For A_S^{ss}, $\boldsymbol{h}_{1\to2} = a(\hat{\boldsymbol{r}}_2 - \hat{\boldsymbol{r}}_1) + (z_2 - z_1)\hat{\boldsymbol{z}}$, where, $\hat{\boldsymbol{r}}_1 = \cos\theta_1\hat{\boldsymbol{x}} + \sin\theta_1\hat{\boldsymbol{y}}$, and, $\hat{\boldsymbol{r}}_2 = \cos\theta_2\hat{\boldsymbol{x}} + \sin\theta_2\hat{\boldsymbol{y}}$. The inward surface normal unit vectors from dA_1 and dA_2 are $-\hat{\boldsymbol{r}}_1$ and $-\hat{\boldsymbol{r}}_2$, respectively. The vector from the point source to dA_1 is $\boldsymbol{r} = a\hat{\boldsymbol{r}}_1 + z_1\hat{\boldsymbol{z}} - \boldsymbol{r}_0$. Using (4), A_S^{ss} may be written

$$A_S^{ss} = -\frac{r_0^2}{4\pi V_{cav}} \int \frac{dA_1}{|\boldsymbol{r}|^3} \int dA_2 \frac{(\hat{\boldsymbol{r}}_1 \cdot \boldsymbol{h}_{1\to2})(\hat{\boldsymbol{r}}_2 \cdot \boldsymbol{h}_{1\to2})(\boldsymbol{r} \cdot \boldsymbol{h}_{1\to2})}{h^4} \tag{A.1}$$

where $h = |\boldsymbol{h}_{1\to2}| = |\boldsymbol{h}_{2\to1}|$. The volume of the cavity is $V_{cav} = 2\pi a^2 L$. Substitution by the expressions in the text preceding (A.1) gives

$$A_S^{ss} = -\frac{r_0^2}{8\pi^2 a^2 L} \int_0^{2\pi} ad\theta_1 \int_{-L}^{L} dz_1 \frac{1}{(r_0^2 - 2ar_0\sin\theta_1 + a^2 + z_1^2)^{3/2}} \int_0^{2\pi} ad\theta_2 \int_{-L}^{L} dz_2$$
$$\times \frac{a^2[1-\cos(\theta_2-\theta_1)]^2\{r_0 a(\sin\theta_2 - \sin\theta_1) + a^2[1-\cos(\theta_2-\theta_1)] - z_1(z_2-z_1)\}}{\{2a^2[1-\cos(\theta_2-\theta_1)] + (z_2-z_1)^2\}^2}. \tag{A.2}$$

Make the rotation $\theta_2 \to \theta_2 + \theta_1$, effectively aligning the axes of the two integrations. Substitution of integration variables is always valid. A term proportional to $\sin\theta_2$ vanishes, by symmetry. Then, defining the dimensionless variables, $x = z_1/L$, $y = z_2/L$, $\sigma = a/L$, and $\alpha = a/r_0$, the following may be obtained:

$$A_S^{ss} = \int_{-1}^{1} dx \left(G_{1a}(x,\alpha,\sigma) \int_{-1}^{1} dy\, f_{1a}(x,y,\sigma) + G_{1b}(x,\alpha,\sigma) \int_{-1}^{1} dy\, f_{1b}(x,y,\sigma) \right) \tag{A.3}$$

where

$$G_{1a}(x,\alpha,\sigma) = \frac{1}{2\pi} \int_0^{2\pi} d\theta_1 \frac{\sin\theta_1 - \alpha}{(1 - 2\alpha\sin\theta_1 + \alpha^2 + \alpha^2x^2/\sigma^2)^{3/2}} \tag{A.4}$$

$$G_{1b}(x,\alpha,\sigma) = \frac{1}{2\pi} \int_0^{2\pi} d\theta_1 \frac{\alpha}{(1 - 2\alpha\sin\theta_1 + \alpha^2 + \alpha^2x^2/\sigma^2)^{3/2}} \tag{A.5}$$

$$f_{1a}(x,y,\sigma) = \frac{\sigma^3}{4\pi} \int_0^{2\pi} d\theta_2 \frac{(1-\cos\theta_2)^3}{[2\sigma^2(1-\cos\theta_2) + (y-x)^2]^2} \tag{A.6}$$

$$f_{1b}(x,y,\sigma) = \frac{\sigma}{4\pi} x(y-x) \int_0^{2\pi} d\theta_2 \frac{(1-\cos\theta_2)^2}{[2\sigma^2(1-\cos\theta_2) + (y-x)^2]^2}. \tag{A.7}$$

Starting with G_{1b} in (A.5), one may employ the periodicity of the trigonometric functions and the trigonometric identity, $\cos 2\theta = 2\cos^2\theta - 1$ to obtain

$$G_{1b}(x,\alpha,\sigma) = \frac{2\alpha}{\pi} \int_0^{\pi/2} d\theta\, [(1+\alpha)^2 + \alpha^2x^2/\sigma^2 - 4\alpha\sin^2\theta]^{-3/2} \tag{A.8}$$

or

$$G_{1b}(x,\alpha,\sigma) = \frac{q^3}{8\alpha^{\frac{1}{2}}} \frac{2}{\pi} \int_0^{\pi/2} d\theta\, (1 - q^2\sin^2\theta)^{-3/2} = \frac{q^3}{8\alpha^{\frac{1}{2}}} \Pi_0(q^2, q) \tag{A.9}$$

where $\Pi_0(q^2, q)$ is given in (9) and q is given in (10). Similar manipulations lead to the form for G_{1a} given in (8)–(10).

To obtain explicit forms for f_{1a} and f_{1b}, consider the auxiliary function

$$I(u,v) = \frac{1}{2\pi}\int_0^{2\pi} d\theta \frac{(1-\cos\theta)^2}{u(1-\cos\theta)+v} \tag{A.10}$$

which is easily integrated to give

$$I(u,v) = \left(\frac{1}{u} - \frac{v}{u^2} + \frac{v^2}{u^2[v(2u+v)]^{1/2}}\right). \tag{A.11}$$

From (A.6), (A.7) and (A.10) one sees that f_{1a} and f_{1b} can be obtained from derivatives of the auxiliary function $I(u,v)$. That is,

$$f_{1a}(x,y,\sigma) = -\frac{\sigma^3}{2}\frac{\partial}{\partial u} I(u,v)\Big|_{\substack{u=2\sigma^2 \\ v=(y-x)^2}} \tag{A.12}$$

$$f_{1b}(x,y,\sigma) = -\frac{\sigma}{2}x(y-x)\frac{\partial}{\partial v} I(u,v)\Big|_{\substack{u=2\sigma^2 \\ v=(y-x)^2}} \tag{A.13}$$

The derivatives may be evaluated straightforwardly with the result,

$$f_{1a}(x,y,\sigma) = \frac{1}{8\sigma}\left[1 - \frac{(x-y)^2}{\sigma^2}\left(1 - \frac{|x-y|[5\sigma^2+(x-y)^2]}{[4\sigma^2+(x-y)^2]^{3/2}}\right)\right] \tag{A.14}$$

$$f_{1b}(x,y,\sigma) = \frac{x(y-x)}{8\sigma^3}\left(1 - \frac{|x-y|[6\sigma^2+(x-y)^2]}{[4\sigma^2+(x-y)^2]^{3/2}}\right). \tag{A.15}$$

Résumé

Théorie analytique du facteur de correction de non uniformité avec une source ponctuelle, pour des chambres d'ionisation à paroi épaisse dans des faisceaux de photons.

Pour les mesures d'exposition et de kerma dans l'air, on utilise des facteurs de correction de perturbation axiale et radiale correspondant à la non uniformité du champ de photons incidents au voisinage de la cavité de la chambre d'ionisation. Les auteurs présentent une théorie analytique permettant de calculer le facteur de correction pour la non uniformité avec une source ponctuelle, s'appliquant aux chambres d'ionisation à paroi épaisse. La théorie présentée dans ce travail est comparée aux calculs effectués selon la méthode de Monte Carlo pour des chambres de géometrés planes, cylindriques et sphériques, de taille comparable à celle des détecteurs utilisés par les laboratoires d'étalonnage. L'accord observé entre les calculs par la méthode de Monte Carlo et la théorie analytique est excellent et démontre la validité de la théorie analytique pour les grandes et petites distances source–chambre. Les auteurs suggèrent que les corrections à appliquer pour ces perturbations, qui diffèrent de celles calculées ou mesurées par quelques laboratoires d'etallonage, sont de l'ordre de 0.3% pour les chambres de géométrie plane typiques, sont petites et de l'ordre de 0.05% ou moins pour les chambres type Farmer usuelles, et sont nulles pour les chambres sphériques. La théorie analytique permet de prévoir des géométries de chambre permettant soit de réduire soit d'augmenter l'effet de non uniformité avec les sources ponctuelles. Enfin, les auteurs décrivent une expérience destinée à fournir la mesure de cette correction avec une bonne précision.

Zusammenfassung

Eine analytische Theorie des Punktquellen-Inhomogenitätskorrektionsfaktors für dickwandige Ionisationskammern in Photonenstrahlen.

Bei Messungen der Ionendosis und der Kerma in Luft werden axiale und radiale Inhomogenitätskorrektionsfaktoren zur Berücksichtigung der Non-Uniformität des einfallenden Photonenfeldes in der Nähe des Ionisationskammerhohlraumes verwendet. Eine analytische Theorie zur Berechnung des Punktquellen-Inhomogenitätskorrektionsfaktors fur dickwandige Ionisationskammern wurde entwickelt. Die zugrundeliegende Theorie wird verglichen mit Monte Carlo-Rechnungen für Flachkammern und Kammern mit Zylinder- und Kugelgeometrie ähnlich groß wie die von den Standardlaboratorien verwendeten Geräte. Die Übereinstimmung zwischen Monto Carlo-Berechnungen und analytischer Theorie ist hervorragend und zeigt die Bedeutung der analytischen Theorie bei großen und kleinen Quelle-Kammer-Abständen. Die Störungen, die sich von den berechneten oder gemessenen Werten einiger Standardlaboratorien unterscheiden, legen nahe, Korrekturen in Höhe von 0.3% bei Flachkammern zu verwenden, kleinere Korrekturen in Höhe von 0.05% oder weniger bei Farmerkammern und keinerlei Korrekturen bei Kugelkammern. Die analytische Geometrie sagt Kammergeometrien voraus, die den Effekt der Punktquelleninhomogenität entweder verkleinern oder vergrößern. Ein Experiment wird beschrieben, mit dessen Hilfe die Korrekturen mit großer Genauigkeit gemessen werden können.

References

de Almeida C E and Niatel M-T 1986 *Comparison between IRD and BIPM Exposure and Air-Kerma Standards* BIPM Report BIPM-86/12 (Sèvres:BIPM)

Bielajew A F 1986 Ionization cavity theory—a formal derivation of perturbation factors for thick-walled ion chambers in photon beams *Phys. Med. Biol.* **30** 161–70

—— 1990 Correction factors for thick-walled ionisation chambers in point-source photon beams *Phys. Med. Biol.* **35** 501–16

Bielajew A F and Rogers D W O 1986 *Photoelectron Angular Distribution in the EGS4 Code System* NRCC Report PIRS-0058 (Ottawa: NRCC)

—— 1987 PRESTA—the parameter reduced electron-step transport algorithm for electron Monte Carlo transport *Nucl. Instrum. Methods* **B18** 165–81

Bielajew A F, Rogers D W O and Nahum A E 1985 The Monte Carlo simulation of ion chamber response to ^{60}Co—resolution of anomalies associated with interfaces *Phys. Med. Biol.* **30** 419–27

Boutillon M 1988 *(private communication)*

Boutillon M and Niatel M-T 1973 A study of a graphite chamber for absolute exposure measurements of ^{60}Co gamma rays *Metrologia* **9** 139–46

Burlin T E 1959 The measurement of exposure dose for high energy radiation with cavity ionization chambers *Phys. Med. Biol.* **3** 197–206

Costrell L 1962 Scattered radiation from large ^{137}Cs sources *Health Phys.* **8** 491–8

Failla G and Marinelli L D 1937 The measurement of the ionization produced in air by gamma rays *Am. J. Roentgenol.* **38** 312–43

Fano U 1954 Note on the Bragg-Gray cavity principle for measuring energy dissipation *Radiat. Res.* **1** 237–40

Gray L H 1937 Radiation dosimetry, Part II *Br. J. Radiology* **10** 721–42

Kondo S and Randolph M L 1960 Effect of finite size of ionization chambers on measurements of small photon sources *Radiat. Res.* **13** 37–60

Laitano R F and Toni M P 1983 *The Primary Exposure Standard for Co-60 Gamma Radiation: Characteristics and Measurement Procedures* ENEA Report RT/PROT(82)28 (Casaccia, c.p. 2400 Rome, Italy)

Loftus T P and Weaver J T 1974 Standardization of ^{60}Co and ^{137}Cs gamma-ray beams in terms of exposure *J. Res. National Bureau of Standards* **78A** 465–76

Mayneord W V and Roberts J E 1937 An attempt at precision measurements of gamma rays *Br. J. Radiol.* **10** 365–88

Nelms A T 1953 *Graphs of the Compton Energy–Angle Relationship and the Klein–Nishina Formula from 10 keV to 500 MeV* National Bureau of Standards Circular 542 (Washington, DC:US Government Printing Office)

Nelson W R, Hirayama H and Rogers D W O 1985 *The EGS4 Code System* Stanford Linear Accelerator Report SLAC-265 (Stanford, CA: SLAC)

Niatel M-T, Loftus T P and Oetzmann W 1975 Comparison of exposure standards for ^{60}Co gamma rays *Metrologia* **11** 17–23

Rogers D W O 1984 Low energy electron transport with EGS *Nucl. Instrum. Methods*A **227** 535–48

Rogers D W O and Bielajew A F 1984 *The Use of EGS for Monte Carlo Calculations in Medical Physics* NRCC Report PXNR-2692 (Ottawa: NRCC)

Rogers D W O, Bielajew A F and Nahum A E 1985 Ion chamber response and A_{wall} correction factors in a ^{60}Co beam by Monte Carlo simulation *Phys. Med. Biol.* **30** 429–43

Rogers D W O, Ewart G M, Bielajew A F and Van Dyk G 1988 *Calculation of electron contamination in a ^{60}Co therapy beam, Proc. IAEA Int. Symp. on Dosimetry in Radiotherapy* vol 2, (Vienna: IAEA) pp 303–12

Sauter F 1931 Über den atomaren photoeffekt in der K-schale nach der relativistischen wallenmechanik Diracs *Ann. Phys., Lpz.* **11** 454–88

Shortt K R and Ross C K 1986 *The Canadian ^{60}Co Exposure Standard* NRCC Report PIRS-0052 (Ottawa: NRCC)

Spencer L V and Attix F H 1955 A theory of cavity ionization *Radiat. Res.* **3** 239–54

Spiers F W 1941 Inverse square law errors in gamma-ray dose measurements *Br. J. Radiol.* **14** 147–56